# Electronic relaxation and coherent phonon dynamics in semiconducting single-walled carbon nanotubes with several chiralities

Takayoshi Kobayashi,[1,2,3,4,*] Zhaogang Nie,[1,2,†] Juan Du,[1,2] Kotaro Okamura,[1] Hiromichi Kataura,[5]
Youichi Sakakibara,[6] and Yasumitsu Miyata[7]

[1]*Advanced Ultrafast Laser Research Center and Department of Engineering Science, Faculty of Informatics and Engineering,
University of Electro-Communications, 1-5-1 Chofugaoka, Chofu, Tokyo 182-8585, Japan*
[2]*JST, CREST, 5 Sanbancho, Chiyoda-ku, Tokyo 102-0075, Japan*
[3]*Department of Electrophysics, National Chiao-Tung University, Hsinchu 30010, Taiwan*
[4]*Institute of Laser Engineering, Osaka University, 2-6 Yamada-oka, Suita, Osaka 565-0871, Japan*
[5]*Nanosystem Research Institute, AIST, Higashi 1-1-1, Tsukuba, Ibaraki 305-8562, Japan*
[6]*Nanoelectronics Research Institute, AIST, Umezono 1-1-1, Tsukuba, Ibaraki 305-8568, Japan*
[7]*Department of Chemistry, Nagoya University, Furo-cho, Chikusa-ku, Nagoya, 464-8601, Japan*

Coherent phonon (CP) dynamics and electronic relaxation in single-walled carbon nanotubes (SWNTs) are investigated in femtosecond pump-probe experiments. Using a sensitive multichannel lock-in amplifier, chirality-specific electronic relaxation and vibrational dynamics are resolved in SWNT ensembles composed of several chiral systems without the need for selective isolation of the different species by purification. The dynamics of vibrational wave packets are studied based on oscillatory changes in the absorbance of the systems. Modulations corresponding to the radial breathing mode (RBM), observed in the time traces of the absorbance change for the four chiral systems (6,4), (6,5), (7,5), and (8,3), have been analyzed in detail. The vibrational modes of the CP spectra are identified from the two-dimensional distribution of probe photon energy versus Fourier frequency. Resonance conditions and mode frequencies lead to definite chirality assignments. Coherent RBM phonon generation is analyzed using the probe photon energy-dependent amplitude profiles as a result of the spectral shift induced by wave-packet motion on the potential surface. The present study clarifies that the observed probe photon energy dependence is due to both the imaginary and real parts of the third-order susceptibility, corresponding to Raman (and Raman-like) gain and loss processes and to molecular phase modulation, respectively. The imaginary part is the dominant contribution to the modulation in the difference absorbance. It shows probe photon energy dependence in the form of a difference in absorbed photon energy between the spectra that are shifted and unshifted with vibrational frequency. The size of the Huang-Rhys factors from the difference fitting to the (6,4), (6,5), and (8,3) systems are 0.26, 0.32, and 0.75, respectively. The trend of the factors originates in the stiffness differences of the SWNT structures. The real part depends on the derivative of the absorbed photon energy spectrum due to cross-phase modulation, resulting from the change in refractive index during the molecular vibrations. This process induces a probe spectral change, as evidenced by first-derivative fitting using a small number of data points of probe photon energies. The effective nonlinear refractive index for each chiral system is determined to range from 0.2 to $3.1 \times 10^{-17}$ cm$^2$/W.

## I. INTRODUCTION

Extensive studies have been carried out on carbon nanotubes (CNTs) following their discovery by Iijima in 1991.[1] Nanostructured carbon materials include fullerenes, peapods, graphene, and CNTs. Single-walled carbon nanotubes (SWNTs) with one-dimensional nanostructures have unique mechanical, electronic, and optical properties.[2–4] In particular, depending on their chirality, they can exhibit either metallic or semiconducting characteristics.[5] In addition, their one-dimensional nature, which is similar to materials such as conjugated polymers,[6,7] provides a playground for studying the dynamics of confined electrons and phonons.[8–11] Similar to conjugated polymers, SWNTs exhibit unique vibronic and exciton-phonon couplings.[12,13] Theoretical and experimental studies have revealed a variety of phonon-assisted peaks, suggesting strong exciton-phonon coupling,[14–18] which is often at the heart of many important phenomena in condensed matter physics. Although exciton-phonon coupling in SWNTs

is usually studied by Raman spectroscopy,[19–23] it is only a sensitive probe of ground-state vibrations. Recently, efforts have been made to investigate coherent lattice vibrations (phonons) in SWNTs by coherent phonon (CP) spectroscopy via femtosecond pump-probe techniques, which can also enable direct measurement of time-domain CP dynamics in excited states.[24]

There are two methods of studying the vibrational dynamics in condensed matter. One is in the frequency domain, and the other is in the time domain. The former techniques are more common and include time-resolved Raman scattering or infrared absorption. The latter technique is real-time vibrational spectroscopy, which is used to obtain information about the amplitudes of vibration through a modulation of the electronic transition probabilities. Information can also be obtained about the vibronic coupling strengths and dynamics of the vibrational modes in both the ground and excited electronic states. In this manner, the relaxation of electronic states and the dynamics of vibrational levels can both be

studied using the same experimental equipment under exactly the same conditions. The real-time vibrational spectroscopy has been used for many different molecular, bimolecular, polymer, and biopolymer systems.[25–27]

CP dynamics in SWNTs have been studied by several groups using the impulsive excitation method.[24,28–36] However, there are three important concerns that need to be addressed. The first is the mechanism of the CP generation, which is related to coupling between phonon modes and the electronic structure, resulting in modulation of the probed difference absorbance. Using a tunable laser with a 50-fs pulse duration, Lim *et al.* observed radial breathing mode (RBM) vibrations.[28] The oscillations in the probe transmittance were found to be the result of ultrafast modulation of the optical constants at a frequency $\omega_{\text{RBM}}$ due to bandgap ($E_{\text{gap}}$) oscillations induced by changes in the SWNT diameter $d$ ($E_{\text{gap}} \propto 1/d$). It was claimed that the photon energy dependence of the CP signal shows a first-derivative behavior. Subsequently, Kim *et al.*[29] and Lüer *et al.*[32] drew similar conclusions in their investigations of chiral SWNTs using other experimental schemes. These papers suggested that the CPs induced by femtosecond visible or near-infrared pulses are in the ground states. However, impulsive excitation can also generate CPs in excited states when the femtosecond pulse is resonant with the electronic transition.[24,28–38]

The second concern is that there has been no discussion of the effects of modulation of the phase of the light field, as opposed to that of the molecular vibrations, due to the periodic change in the refractive index of the material. Rapid modulation of the refractive index by molecular vibrations can lead to a spectral shift, leading to spectral changes in the probe due to molecular phase modulation (MPM), which is similar in concept to self-phase modulation[39] and cross-phase modulation.[40]

The third issue is that energy exchange between CPs and the optical field of the probe has not been fully considered. Probe photons with energies higher and lower than some specific spectral component can interact simultaneously with CPs, resulting in a complicated dependence of the CP signal on the probe energy. For example, in the study of Lim *et al.* in 2006,[28] the probe photon energy dependence of the CP signal was investigated using broad probe bandwidths (25 nm or more), and the spectral shape was compared with the absolute value of the first derivative of the absorption spectrum. Although they concluded that the two spectral shapes were similar, their results showed that the CP amplitude profile was much steeper than the derivative-based profile, explained in terms of a band-gap oscillation that induces a shift in the transition absorption spectrum. The separations between the two inflection points and between the two peaks in the CP amplitude are calculated to be about 40 meV and 70 meV, respectively, using Fig. 5 of the paper.[28] The two inflection points and the two derivative peaks should be coincident if the spectral shift is the origin of the oscillating signal. In fact, the two values differ by a factor of more than 1.7 times, and thus the real-time traces cannot simply be explained by the spectral shift mechanism. In 2009, Kim *et al.*[29] studied CNTs by selectively exciting CPs for RBMs in SWNTs using a pulse-shaping technique and measured the probe photon energy dependence of the amplitudes in the same way as Lim *et al.*

From Fig. 4 in Ref. 29, it can be easily seen that the full width at half-maximum (FWHM) of the photoluminescence excitation profile corresponding to the absorption spectrum is ∼55 meV, while that of the reconstructed spectrum calculated from the CP excitation profile is ∼125 meV, which is more than twice as large. In the same year, Lüer *et al.*[32] used sub-10-fs visible pulses and a broadband detector to obtain a nearly continuous spectrum of the probe wavelength dependence of the CP amplitude and phase, based on the time-dependent wave-packet theory of Kumar *et al.*[41,42] The positions of the low- and high-energy peaks and the valley bottom of the modulation depth were found to be 564, 589, and 575 nm, respectively, compared with values of 562, 579, and 571 nm obtained from simulations, as shown in Fig. 5(a) of their paper.[30] The half-widths of the CP amplitude spectrum and of the first-derivative profiles were estimated to be 25 and 17 nm, respectively, from the data of their paper.[30] Thus, the deviation is as large as almost 50%, which is particularly noticeable if the data are displayed on top of each other in the same graph.

The solution to all of these problems is to clarify the mechanism of CP generation in SWNTs. This will aid in the development of new applications of CNTs in optical devices such as capillary containers for small molecules.

In addition, the bond length change associated with CPs results in photoinduced reactions, such as the opening and fragmentation of the end caps of CNTs.[43–45] Such fragmentation is induced by structural transformations triggered by femtosecond laser excitation.[43–45] Dumitrica *et al.*[43,44] demonstrated the possibility of selectively opening a nonequilibrium cap of a CNT after femtosecond excitation. Ultrafast bond weakening and simultaneous excitation of two CP modes with different frequencies, localized in the spherical caps and in the cylindrical nanotube body, are responsible for the selective cap opening. The nanotube radius initially increases due to the induced RBM deformation triggered by the exciton-phonon coupling and then decreases followed by the oscillatory behavior. When the radius becomes larger than that of the enlarged spherical cap at the end of the CNT, bond breaking takes place, causing the cap to open. This photoinduced cap opening is a serious problem for CNT applications because of photostability and robustness issues, as well as for applications involving encapsulation and decapsulation of chemicals in CNTs. The initial phase of the coherent vibrations, particularly the vibrations of RBMs, affects the cap opening. The importance of coherent vibrational modes has been discussed for molecular systems in solution or solid materials including CNTs. For solutions, the mechanism of coherent vibration during a chemical reaction was studied for various molecules.[46,47]

In the present paper, we report a detailed pump-probe study of CPs in SWNTs using sub-10-fs visible pulses. Although many chiral systems coexist in the sample, we can distinguish four different semiconducting systems because of the large bandwidth of the short pulse, extending from the visible to the near infrared, and because of our sensitive broadband detection system. Consequently, we obtain abundant information about the probe photon energy dependence of the phonon amplitudes of the RBMs, leading to an understanding of CP generation. The probe photon amplitude profiles are analyzed in terms of the modulation of the excitonic transition probabilities. Since

the signal from the pump-probe experiment is generated in a third-order nonlinear (NL) process, the real and imaginary parts of the NL susceptibility can both play roles. The effects of the CPs on the difference absorbance are fully modeled. Furthermore, given the importance of the structural response to the impulsive photoexcitation for chiral-selective end functionalization of SWNTs, the electronic origin of tube structural changes is discussed in terms of the first moment of the electronic transition energy associated with the difference absorption. The effect of the refractive index changes associated with the CP vibrations is clarified.

## II. EXPERIMENT

### A. Ultrafast spectroscopy

The pump and probe beams are generated in a non-collinear parametric amplifier (NOPA),[48,49] excited in turn by a commercial regenerative amplifier (Spectra Physics Spitfire). The central wavelength, pulse duration, output power, and repetition rate of the regenerative amplifier are 800 nm, 50 fs, 740 mW, and 5 kHz, respectively. The output from the NOPA spans the spectral range 1.71–2.37 eV (524–723 nm). Using a compression system composed of a pair of prisms and chirped mirrors, 7.1-fs pulses with a constant spectral phase, indicating that they are nearly Fourier-transform (FT) limited, are generated. The pulse energies of the pump and probe are 32 and 6 nJ, respectively. The polarization directions of the pump and probe beams are parallel to each other.

In the experiment, the signal is spectrally dispersed using a polychromator (Jasco M25-TP) into 128 photon energies between 1.71 and 2.37 eV. These beams are detected by 128 sets of avalanche photodiodes and lock-in amplifiers with a reference from an optical chopper intersecting the pump pulse at a 2.5 kHz repetition rate. The experiment is performed at room temperature (293 $\pm$ 1 K).

### B. Sample preparation

A CoMoCAT synthesis is performed using a silica support (Sigma-Aldrich $SiO_2$ with a 6-nm average pore size and a Brunauer-Emmett-Teller [BET] surface area of 480 $m^2$ $g^{-1}$) and a bimetallic catalyst prepared from cobalt nitrate and ammonium heptamolybdate precursors.[50–52] The total metallic loading in the catalyst is 2 wt%, with a Co:Mo molar ratio of 1:3. Before exposure to the Co feedstock, the catalyst is heated to 500 °C in a flow of gaseous $H_2$ and further heated to 750 °C in flowing He. A Co-disproportionation reaction is used to produce SWNTs in a fluidized bed reactor under a flow of pure Co at five atmospheres. The SWNTs grown by this method remain mixed with the spent catalyst, containing the silica support and the Co and Mo species. To eliminate the silica from the mixture, the solid product is suspended in a stirred 20% HF solution for 3 h at 25 °C. The suspension is then filtered through a 0.2-$\mu$m PTFE membrane and washed with deionized water to neutralize it. Next, the solid product is added to an aqueous solution containing the surfactant sodium dodecylbenzene sulfonate at twice the concentration of its critical micelle level, and it is then ultrasonically agitated for 1 h using a Fisher Scientific Model 550 homogenizer (with a 550 W output). This creates a stable suspension of individual and bundled

nanotubes. The suspension is centrifuged for 1 h at 72 600 $g$ to separate metallic catalyst particles and suspended tube bundles from the lower density surfactant-suspended nanotubes. Only a small fraction of the product becomes deposited at the bottom of the centrifuge tube. Finally, the supernatant liquid, enriched in individual surfactant-suspended SWNTs, is withdrawn and adjusted to a pH of between 8 and 9 for spectral analysis.

We have measured morphologies of SWNTs studied in this work using atomic force microscope (AFM) (SII NanoTechnology, S-image). The average length was 330 nm with standard deviation of 160 nm, and the heights were about 1 nm, which is close to the diameter of individual SWNT. The average length was slightly shorter than the original length of CoMoCAT written in the specification, but the shortening should not give serious effects to the optical properties of SWNTs. Although the width of each SWNT was not well known due to the limited horizontal resolution of AFM, the low height means that SWNTs are thought to be well dispersed to almost individuals or at least very thin bundles. Details are described in the Supplemental Material.[53] The samples are then used without further fractionation or extraction.

## III. RESULTS AND DISCUSSION

### A. Stationary absorption spectrum

Figure 1(a) plots the stationary absorption spectrum of the SWNTs with the relevant chirality assigned. There are more than 15 absorption peaks and shoulders in the spectral range 1.22–2.67 eV. In the energy range of our laser spectrum [1.71–2.36 eV, see Fig. 1(b)], the absorption spectrum has three peaks at 2.17, 1.91, and 1.78 eV, which are assigned to the (6,5), (7,5), and (9,1) chiral systems, respectively. There are also two shoulders near 2.10 and 1.85 eV, which are attributed to the (6,4) and (8,3) chiral systems, respectively. This assignment is made based on the published relationship between the transition energy and chiral index set $(n,m)$.[50,54–58] The broadband laser spectrum in the visible region, indicated by the dashed line in Fig. 1(b), is resonant with the second excitonic transitions ($E_{22}$) of the semiconducting tubes, avoiding any possible excitation of metallic tubes ($M_{11}$) at higher energies[59] or the first exciton transition ($E_{11}$) at lower energies. The absorption spectrum is fit to the sum of five Voigt functions (shown in gray), which are convolutions of Gaussian and Lorentzian functions, peaking at 2.17, 2.08, 1.91, 1.84, and 1.78 eV, which correspond to the (6,5), (6,4), (7,5), (8,3), and (9,1) tubes, respectively. The assumption of symmetric Voigt spectral shapes is reasonable because of the much smaller width of the theoretically expected van Hove singularity than that of the observed spectra.[60,61] The spectral shapes and peak photon energies obtained in the simulation are slightly uncertain because of overlap with neighboring peaks. However, the overall spectral positions are estimated to be accurate to less than 5 meV based on the noise level and simulations. Since the (9,1) tubes exhibit only weak absorption, despite the high laser intensity in this spectral region, the stationary absorption spectrum and pump-probe results focus on the other four chiral systems, namely (6,5), (6,4), (7,5), and (8,3).
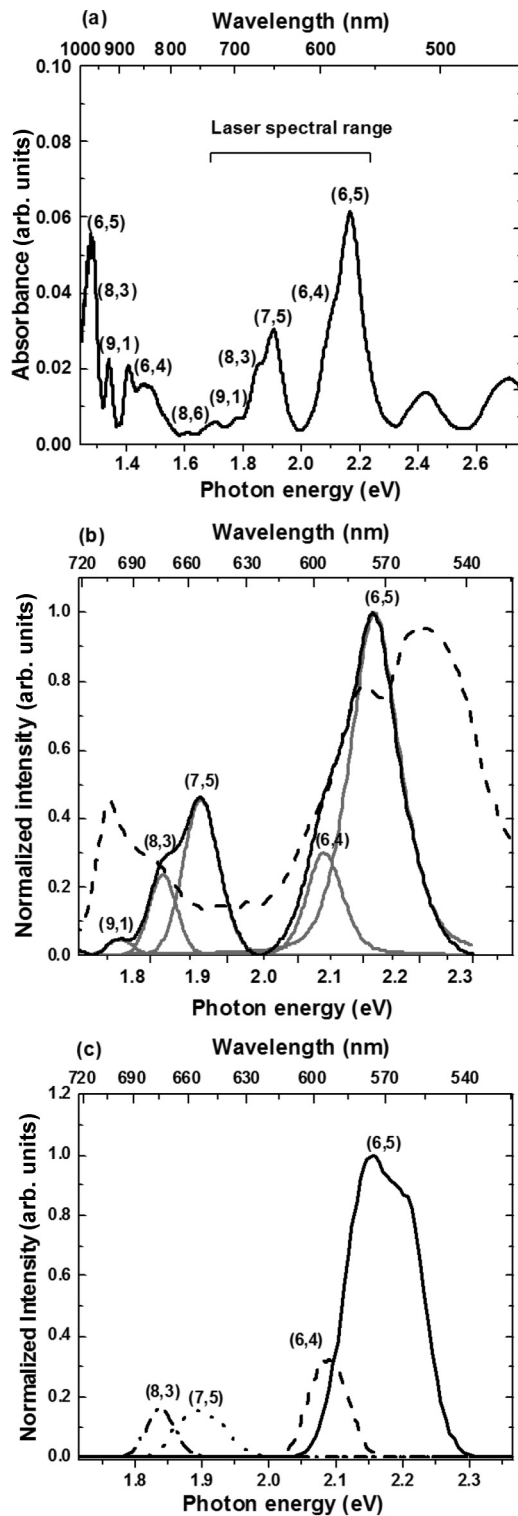
FIG. 1. (a) Stationary absorption spectrum of SWNTs, showing the $E_{11}$ and $E_{22}$ transitions in visible and infrared (1.2–2.7 eV) range. (b) Laser spectrum (dashed line) and stationary visible absorption spectrum of SWNTs (solid line) after subtracting the weak background and its Voigt-fitting profiles (gray lines), illustrating individual $E_{22}$ absorption components in the 1.71–2.36 eV spectral range. The chirality assignments are shown together. (c) Absorbed laser spectra, defined by the difference in the spectrum between the probe light before and after passing thorough the sample, for different chiralities.

Table I lists the fitted widths of the Gaussians and Lorentzians used in the Voigt functions. It is assumed that these widths are due to inhomogeneous and homogeneous broadening, respectively. Accordingly, the homogeneous and inhomogeneous widths of each component can be estimated, as listed in Table I. The four chiral systems have similar inhomogeneous widths of 45–85 meV, while the homogeneous widths vary from 4 to 26 meV, corresponding to a dephasing time of 17–120 fs. The shorter dephasing times are for the broader 26.3 and 22.8 meV homogeneous widths for the (6,5) and (6,4) chiral systems, respectively, which have higher transition energies than the other systems. These shorter dephasing times probably arise from the phase relaxation induced by the interaction between higher vibrational levels that are almost resonant with neighboring chiral systems of lower electronic energy. Given that the lineshape of the laser spectrum can affect the amount of laser energy absorbed, the "absorbed photon energy spectrum"[25,26] is calculated as shown in Fig. 1(c). It is defined as the difference in the spectrum of the probe light before and after passing through the sample. The application of the absorbed photon energy spectrum will be discussed later when considering successful fitting of the experimental results for the dependence of the vibrational amplitude on the probe photon energy, referred to as the probe amplitude spectrum for CPs.

## B. Electronic relaxation and thermalization of excited population

Figure 2(a) graphs the two-dimensional (2D) difference absorption spectra $\Delta A$ plotted against the probe photon energy $E_{\mathrm{pr}}$ and the delay time $t$. The striped oscillatory structures parallel to the time axis represent the modulation of the difference absorbance $\delta \Delta A(E_{\mathrm{pr}}, t)$ by CPs. Here $\delta$ is the modulation of the absorbance change $\Delta A(E_{\mathrm{pr}}, t)$ due to CPs at a specific probe photon energy $E_{\mathrm{pr}}$ and delay time $t$ induced by the spectral shift and transition probability change, which give rise to the horizontal and vertical modulation, respectively. Figure 2(b) plots time-resolved spectra integrated over 200-fs delay-time steps at 10 center-probe delay times ranging from 50 to 1850 fs. There are four prominent bleaching bands composed of three peaks and one shoulder, nearly coincident with the relevant $E_{22}$ transitions for the (6,5), (6,4), (7,5), and (8,3) chiral systems in Fig. 1. In addition, there are three isosbestic points near 2.21, 2.02, and 1.94 eV at delay times longer than 250 fs, as indicated by the small squares. Figure 2(c) expands the spectra near the isosbestic points over a 0–400 fs range with an integration step of 50 fs. The crossing points between neighboring time-resolved spectra are within ±0.03 eV of the average photon energies, except between 0 and 50 fs. Therefore, the relaxation after 200 fs can be described using a simple two-state model composed of a single intermediate state or excited state after photoexcitation, where a conversion from one state to the other is occurring. This behavior can be explained in terms of intraband relaxation from the $E_{22}$ excitonic state to the $E_{11}$ excitonic state, followed by a slower decay from $E_{11}$ to the ground state. Moreover, Fig. 2(a) shows that the zero-crossing photon energy rapidly changes just after excitation until a probe delay time of 300 fs, after which the change slows down. The mean rates of change

TABLE I. Observed absorption band width and band center and fitted parameter with a Voigt function. $\sigma$ (meV): Gaussian width; $\gamma$ (meV): Lorentzian width; $f_{G}$ (meV): FWHM of the Gaussian profile; $f_{L}$ (meV): FWHM of the Lorentzian profile; $f_{v}$ (meV): FWHM of the Voigt profile.

| Chirality | Center (eV) | FWHM (meV) | $\sigma$ (meV) | $\gamma$ (meV) | $f_{G}$ (meV) | $f_{L}$ (meV) | $f_{v}$ (meV) | $L_{G}$ (fs) | $L_{L}$ (fs) |
|---|---|---|---|---|---|---|---|---|---|
| (6,5) | 2.17 | 89.9 | 36.1 | 13.1 | 84.9 | 26.3 | 97.4 | 21.5 | 17.0 |
| (6,4) | 2.09 | 64.6 | 19.2 | 11.4 | 45.1 | 22.8 | 58.1 | 40.4 | 19.9 |
| (7,5) | 1.91 | 63.9 | 27.4 | 1.88 | 64.6 | 3.96 | 66.7 | 28.2 | 114 |
| (8,3) | 1.84 | 49.2 | 19.9 | 1.87 | 46.9 | 3.76 | 48.9 | 38.9 | 121 |

for the crossing points before and after 300 fs are 82 meV/ps and 7.7 meV/ps, respectively.

Figure 3 displays the electronic decay dynamics of transient absorbance changes probed at 10 different probe photon energies. The relaxation can be fit in all cases by the sum of two exponential functions plus a long lifetime component. The two resulting time constants are listed in Table II. When the probe photons are resonant with the tube absorption, the population signal exhibits an initially rapid partial recovery of the photobleaching and photoinduced absorption ($\tau_1$ ranging from 50–90 fs), followed by slower recovery and growth processes ($\tau_2$ ranging from 600–850 fs) akin to previous results ($\tau_1 < 100$ fs and $\tau_2 \approx 1$ ps) obtained using longer pulses for less dispersed samples.[24,32] Both decay times are shorter for (6,5) and (6,4) than for (7,5) and (8,3) chiral systems, similar to the reduction of the homogeneous dephasing times discussed above.

The decrease in the absolute value of $\Delta A$ can either be due to bleaching recovery or to growth of induced absorption. Positive and negative absorbance changes have been previously observed in two-color pump-probe experiments by Lauret *et al.*[62] The relaxation that occurred over a long period of 1 ps was fit using a power law-decay $t^{-0.5}$. This was explained in terms of a random walk along a one-dimensional CNT chain followed by disappearance due to trapping by defects.[36] However, such a random-walk description is only valid after a few instances of hopping.

### C. FT spectra and chirality assignments

Eight typical real-time traces in the photon energy range of 1.77–2.21 eV are displayed in Fig. 4(a). Figure 4(b) plots the corresponding FT spectra. The calculations are performed on the data after 50 fs to avoid interference near zero time delay. The FT plots show two vibrational modes due to RBMs at $\sim 300$ cm$^{-1}$ ($\sim 100$ fs) and to G modes at 1587 cm$^{-1}$ (21 fs),[24,31,32] generated by the impulsive excitation for a pulse duration (less than 10 fs) much shorter than all of the vibrational periods. Other vibrational modes are too weak to be resolved.

A 2D map of the Fourier power plotted against the probe photon energy and the vibrational frequency is presented in Fig. 5. Four RBMs are evident with vibrational frequencies of about 337, 310, 301, and 282 cm$^{-1}$. The assignment of chirality using only the electronic absorption or Raman spectra is often ambiguous due to spectral congestion.[54–58] In contrast, the intensity of the four dominant double-peaked structures indicated by the double-headed arrows in Fig. 5 corresponds to the first derivative of the electronic absorption spectrum

for the different types of tubes.[28,29,32] The central dip in each structure represents the $E_{22}$ transition, since the oscillation is minimal at resonance.[32] However, as will be discussed later, some corrections must be made to this assertion.

The Raman shifts for different RBMs theoretically correspond to the vibrational frequencies of the FT of their CP profiles.[54,55] Consequently, the dips at the intersections of the horizontal and vertical lines in Fig. 5 correspond to the relevant vibrational frequency and electronic resonance transition energy. Using this relationship, the chirality can be assigned for the (6,4), (6,5), (7,5), and (8,3) systems, as indicated in Fig. 5, because only these tubes can simultaneously fulfill these two conditions. Other kinds of tubes may have weak absorption lines in the laser spectral range, but they cannot be efficiently excited. Using broadband high-sensitivity multichannel lock-in detectors, the power spectra of the four systems can be uniquely distinguished for RBMs, even though their absorption spectra overlap as shown in Fig. 1, without the need for time-consuming or complex pulse-shaping techniques.[29] Therefore, this method is advantageous for simultaneous analysis of a sample containing many chiral systems. However, the dip position and the peak of the absorption spectrum do not exactly coincide, as will be discussed later. In contrast, for G-mode vibrations, the amplitude profiles for different chiralities overlap and cannot be distinguished. The frequency of the axial G-mode is insensitive to the diameter and chirality of SWNTs and is thus not reflected in the location of the signal in Fig. 5.

### D. CP amplitudes of chiral systems

The CP amplitude $Q(t)$ of CNTs induced impulsively by ultrashort optical pulses is approximately represented by

$$Q(t) = Q_e(t) + Q_v(t) \cos(\omega_v t + \phi), \qquad (1)$$

where

$$Q_e(t) = Q_{\rm ex} - Q_{\rm gr} \quad \text{for} \quad t > 0, \quad \text{and}$$
$$Q_e(t) = 0 \quad \text{for} \quad t < 0. \qquad (2)$$

Here $Q_e(t)$ is the difference in the equilibrium position of the phonon coordinate between the electronic ground state $Q_{\rm gr}$ and the exciton state $Q_{\rm ex}$, and it has a short rising part due to the finite pump pulse width. The second term on the right-hand side of Eq. (1) is the product of the envelope vibrational amplitude $Q_v(t)$ and the oscillation with a frequency $\omega_v$ and an initial phase $\phi$. The time dependence of $Q_v(t)$ is due to homogeneous and inhomogeneous vibrational dephasing. Figure 19 in the article by Sanders *et al.*[30] shows that $0 > Q_e(t)$
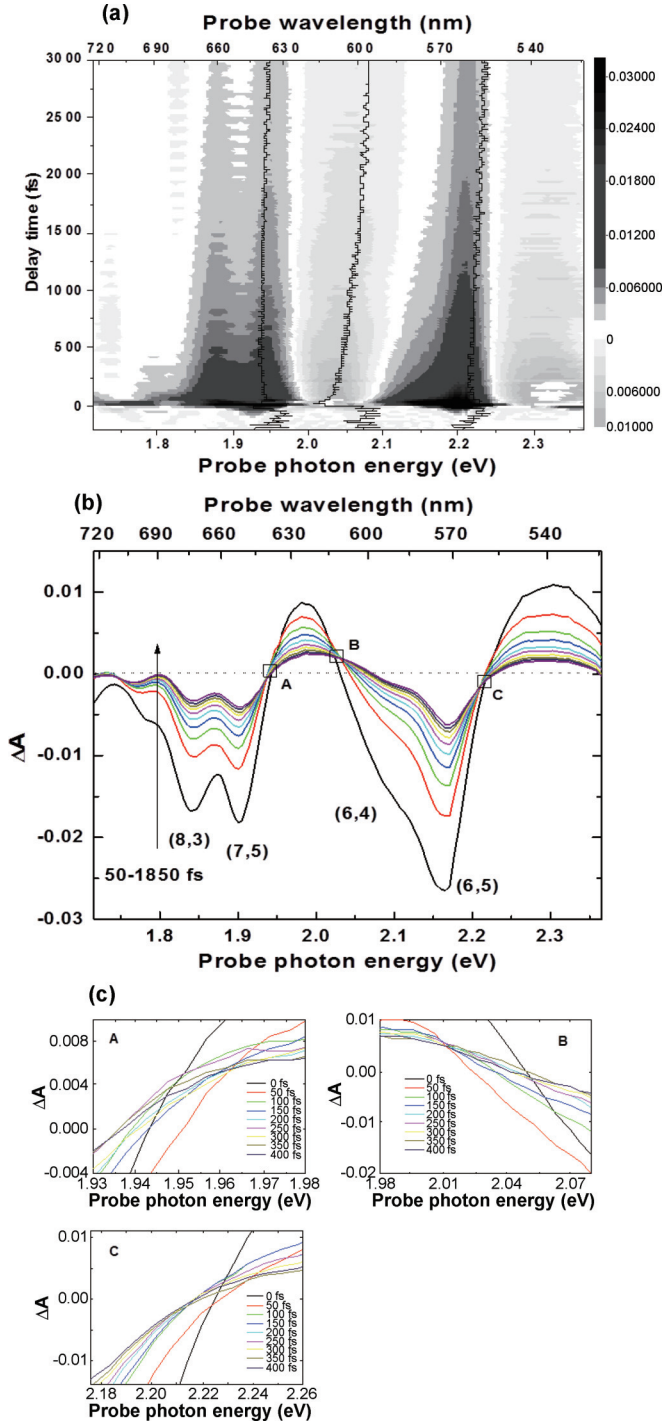
FIG. 2. (Color online) (a) 2D display of $\Delta A$ ($E_{\rm pr}, t$) as functions of probe photon energy, $E_{\rm pr}$, and probe delay time, $t$. The black solid curves are the zero-change lines in the absorbance ($\Delta A = 0$). (b) Time-resolved $\Delta A$ spectra at the delay time points from 50 fs to 1850 fs with a 200-fs integration step. (c) The enlargements of the three isosbestic point regions, shown in the three insets of (b), at around (A) 2.21 eV, (B) 2.03 eV, and (C) 1.93 eV with a 50-fs integration step.

and $|Q_e(t)| > Q_v > 0$ for positive times $t$. The phases were predicted such that $\phi = 0$ for $E_{11}$ transitions in mod 2 CNTs and for $E_{22}$ transitions in mod 1 CNTs, and $\phi = \pi$ for $E_{11}$

transitions in mod 1 CNTs and for $E_{22}$ transitions in mod 2 CNTs.

The four $E_{22}$ CP intensities $I_{(n,m)}$ are plotted in terms of their chirality in Fig. 6. Here, the CP intensities are normalized by the absorbed light intensity, given by the overlap of the laser spectrum and the corresponding Voigt components for the chiral systems in Fig. 1(b). The intensities $I_{(n,m)}$ of the $(n, m)$ systems are in the order $I_{(8,3)} > I_{(7,5)} > I_{(6,4)} > I_{(6,5)}$. This trend is consistent with that predicted by a new microscopic theory describing the generation and detection of CPs in SWNTs, developed by Sanders *et al.*[30] For the RBM modes, they argue that (i) the $E_{22}$ CP intensity decreases with increasing chiral angle $\theta_{(n,m)}$ for a given value of $(2n + m)$; (ii) as the family index increases, the $E_{22}$ CP intensity increases if $(n - m)$ mod 3 equals 1 or 2; and (iii) the CP intensities of mod 1 tubes are considerably weaker than those of mod 2 tubes. In our case, $I_{(8,3)}$ is expected to be more intense than $I_{(7,5)}$ because $\theta_{(8,3)} < \theta_{(7,5)}$. Both of these tubes have the same family index of $2n + m = 19$. Second, tubes (6,4), (7,5), and (8,3) are all mod 2, and $I_{(6,4)}$ is the smallest among the three tubes because the family index of 16 for (6,4) is smaller than that for (7,5) and (8,3). Moreover, according to the new theory, since tube (6,5) is in the mod 1 group and the other three tubes belong to the mod 2 group, $I_{(6,5)}$ should be the smallest among the four tube types.

### E. Raman processes in a classical model

To understand the origin of the oscillatory signal in the real-time traces, we first consider a classical model involving coupled equations describing CPs for two pulsed beams at different frequencies. When an ultrashort pulse with a broad spectrum is used for pumping, two sets of electric fields are involved: $E_{\rm L}$ and $E_{\rm S}$, and $E_{\rm L}$ and $E_{\rm AS}$. The difference between $\omega_{\rm L}$ and $\omega_{\rm S}$ corresponds to the molecular vibrational frequency $\omega_v$. The stimulated Raman process is described by the following set of coupled differential equations in terms of the normal coordinate $Q$ of the molecular vibration,[63]

$$\frac{\partial}{\partial x'} E_{\rm S} = \kappa_{1S} E_{\rm L} Q^*, \tag{3}$$

$$\frac{\partial}{\partial x'} E_{\rm L} = \kappa_{1S} E_{\rm S} Q + \kappa_{1A} E_{\rm AS} Q^*, \tag{4}$$

$$\frac{\partial}{\partial x'} E_{\rm AS} = \kappa_{1A} E_{\rm L} Q, \tag{5}$$

$$\left(\frac{\partial}{\partial t'} + \frac{1}{T_{2v}}\right) Q = \kappa_{2S} E_{\rm L} E_{\rm S}^* + \kappa_{2A} E_{\rm AS} E_{\rm L}^*. \tag{6}$$

Here, $T_{2v}$ is the vibrational phase (transverse) relaxation time including inhomogeneity. The constants $\kappa_{1A}$ and $\kappa_{1S}$ are the coupling strengths of the laser and the Stokes field with CPs, respectively, while the constants $\kappa_{2A}$ and $\kappa_{2S}$ are those between the laser and the anti-Stokes field and between the laser and the Stokes field, respectively. In these equations, it is assumed that there are no spectrally overlapped components at $\omega_{\rm L} - \omega_v$ nor at $\omega_{\rm L} + \omega_v$, which correspond to the downshifted frequency of the Stokes field $E_{\rm S}$ and to the upshifted anti-Stokes field $E_{\rm AS}$, respectively. Equations (3)–(5) determine the spatial variation of the fields $E_{\rm A}$, $E_{\rm L}$, and $E_{\rm AS}$ and of the coherent vibrational amplitude $Q$ in a sample along the propagation direction of the laser beam. Equation (6) describes the dynamics of the
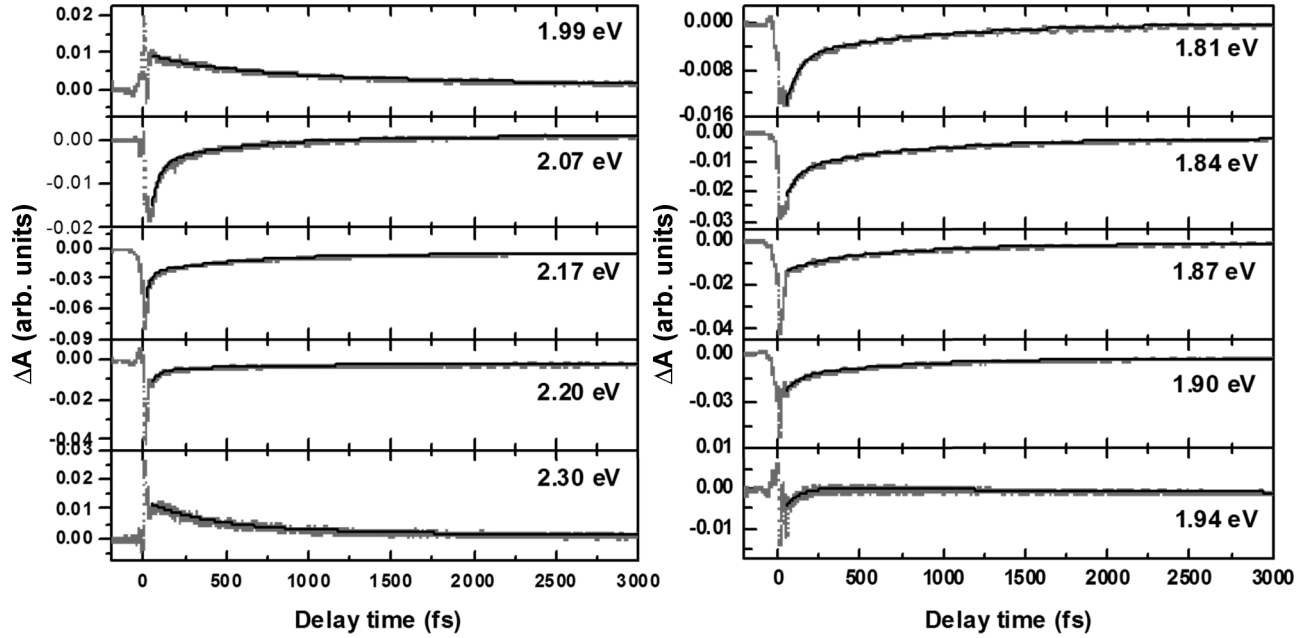
FIG. 3. Electronic decay dynamics of transient absorbance change, probed at 10 probe photon energies (gray dotted lines). The electronic relaxations are expressed by two-order exponential functions plus very long lifetimes (black solid lines). The relevant fitting parameters are shown in Table III.

phonons driven by the pair of fields $E_L$ and $E_S$ and by the pair $E_L$ and $E_{AS}$. After the generation of a CP by a pump pulse, the probe pulse interacts with the coherent vibration. In this process, the coherent vibration with an amplitude $Q$ interacts with the fields $E_L$ and $E_S$ (or $E_{AS}$), as expressed in Eqs. (3)–(5). Thus, these equations allow the spectral dynamics in the time-resolved spectrum to be clearly understood. However, they do not consider the electronic and molecular vibrational energy structure. To take the vibrational energy of a CP into account, a coherent vibration can be modeled as a harmonic oscillator. Furthermore, quantization of the CP coupled exciton needs to be considered. In the following, quantization of electronic and vibrational excitations is described using a semiclassical model in which the optical field remains classical. This model is appropriate because the pump laser field is strong and the effect of the vacuum of the phonon field inducing spontaneous phonon emission by the Raman scattering process can be neglected. The probe is much weaker than the pump, but it is still strong enough for the signal to neglect any detectable spontaneous Raman or electronic emissions, which are emitted over a wide solid angle of $4\pi$ steradians and have a dipolar angular dependence.

TABLE II. Fitting parameters with the two-exponential function for the time traces displayed in Fig. 3.

| $h\nu_{Probe}$ (eV) | Chirality | $a_1$ | $\tau_1$ (fs) | $a_2$ | $\tau_2$ (fs) | $c$ |
|---|---|---|---|---|---|---|
| 1.81 | (8,3) | −0.017 | 70.7 | −0.006 | 838 | −7E-5 |
| 1.84 | (7,5) | −0.016 | 91.2 | −0.010 | 877 | −0.002 |
| 1.90 | (7,5) | −0.014 | 87.0 | −0.012 | 730 | −0.003 |
| 2.07 | (6,4) | −0.023 | 53.4 | −0.006 | 602 | 8E-4 |
| 2.17 | (6,5) | −0.017 | 96.5 | −0.016 | 796 | −0.005 |
| 2.20 | (6,5) | −0.012 | 62.8 | −0.003 | 730 | −0.002 |

### F. Raman and Raman-like processes in a semiclassical model

The laser field is treated classically, whereas the CNT is modeled quantum mechanically using a diagram scheme. The wave packet can be generated either by simultaneous coherent excitation of the vibronic polarization of several vibrational levels in the electronic or excitonic excited states or by impulsively stimulated Raman scattering in the ground state. The former involves a split-excited state, which can be represented in terms of the V-type interaction. Analogously, the latter case requires a split-ground state, expressed as the $\Lambda$-type interaction displayed in Fig. 7(a). Since more than one vibrational level can be excited, at least two levels in both the ground and excited states must be taken into account. As displayed in Fig. 7(b), we include three levels in the ground state, $|g_0\rangle$, $|g_v\rangle$, and $|g_{2v}\rangle$ with energies $E_0$, $E_0 + E_v$, and $E_0 + 2E_v$, respectively, and two levels in the excited state, $|e_0\rangle$ and $|e_v\rangle$ with energies $E_e$ and $E_e + E_v$, respectively. The third electronic state, $|e_{2v}\rangle$, which is not necessarily the second excited state but could instead be a higher excited state, is located near an energy of $2E_e$. In the V-type interaction, two light fields with photon energies of $E_e$ and $E_e + E_v$ interact with the vibrational coherent polarization in the excited states, whereas in the $\Lambda$-type interaction, two fields with photon energies of $E_0$ and $E_0 + E_v$ interact with the vibrational polarization in the ground states.

Figure 8 shows the relevant double-sided Feynman diagrams for NL processes in a four-level system, corresponding to the processes induced by ground state vibrational coherence due to a stimulated Raman process. The two fundamental NL processes A and B are depicted in Eqs. (1) and (2). Processes A and A′ describe the amplitude distributions at low and high energies, respectively, whereas processes B and B′ correspond to vibrational signals at intermediate energy. Diagrams (1), (3), (5), (7), (9), and (12) are due to NL process A/A′, while
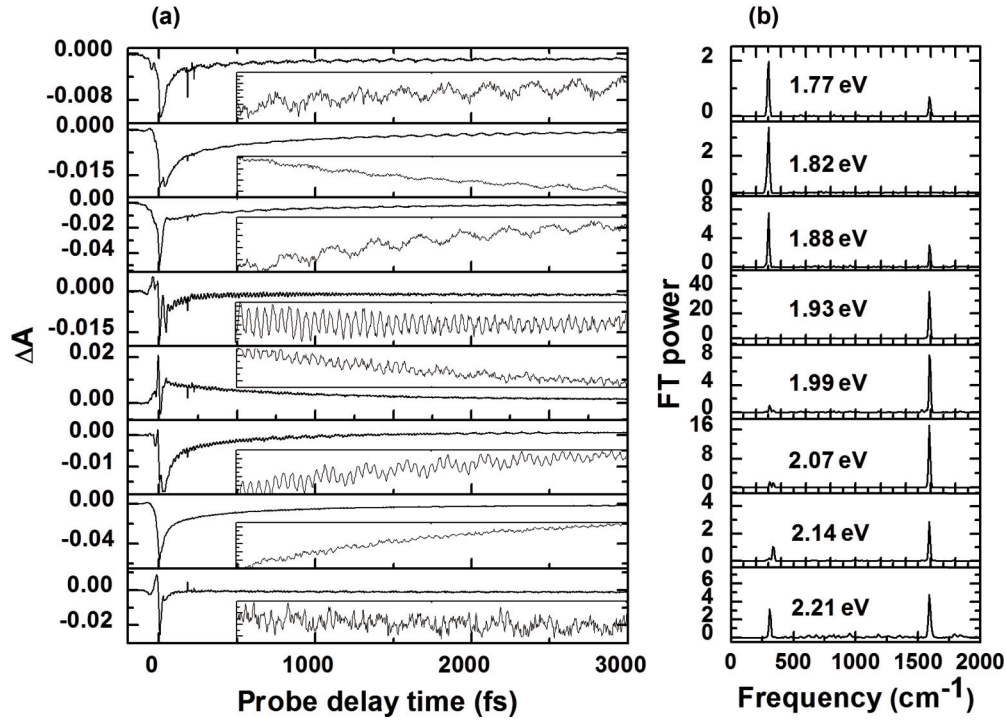
FIG. 4. (a) Real-time traces of the absorbance changes from $-200$ to 3000 fs at eight typical probe photon energies and (b) their corresponding FT power spectra. The insets in (a) are the enlarged real-time traces in 500–1500 fs range showing the pronounced vibrations.

the others are due to B/B′. Feynman diagrams (3)–(6) and (9)–(12) involve a vibrational quantum number of 2.

Before discussing the origins of CPs in SWNTs in detail, we first consider the mechanism for the appearance of the signals. According to the 2D FT power spectrum in Fig. 5, the power of RBMs is weak at photon energies corresponding to the center of the "absorbed spectrum" for the different chiral systems. Although the exact chirality is difficult to assign for G-mode vibrations, the vibrational spectra have two main components, which are outlined in Fig. 5 with a circular ring (upper panel). They display a similar probe photon energy dependence to that previously reported for a highly purified sample CNT sample with a (6,5) chirality.[32] Here, as discussed previously in Refs. [26] and [27], a similar method is used to analyze the ground state NL processes A and B. The phase relations are

$$\phi_{A'}(\omega_v, \omega) = \arctan\left(\frac{-\omega + \omega_0 + \omega_v}{\gamma_2}\right), \quad (7)$$

$$\phi_{B'}(\omega_v, \omega) = \arctan\left(\frac{\omega - \omega_0}{\gamma_2}\right), \quad (8)$$

$$\phi_{A}(\omega_v, \omega) = \arctan\left(\frac{\omega - \omega_0 + \omega_v}{\gamma_2}\right), \quad (9)$$

$$\phi_{B}(\omega_v, \omega) = \arctan\left(\frac{-\omega + \omega_0}{\gamma_2}\right). \quad (10)$$

The frequencies $\omega_0$ and $\omega_v$ correspond to the electronic 0–0 transition and vibrational frequency of the system, respectively. As expressed in Eqs. (8) and (10), the phases of processes B and B′ are opposite, which suggests that the intensity of NL process B will decrease if the intensity of process B′ increases. Since both lie in the same spectral range,

the result of this antiphase relation is that the vibrational spectra, due to these two processes, will cancel each other. A similar phenomenon has been observed for impulsively excited coherent vibrations in chlorophyll.[64]
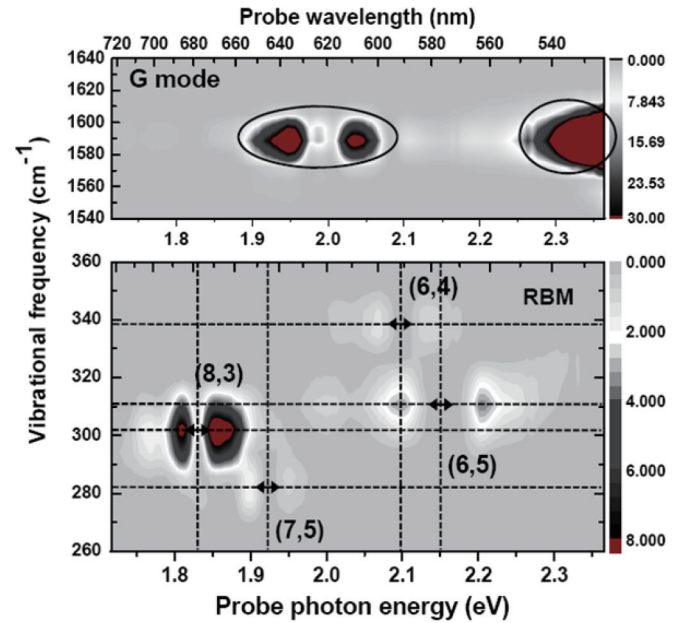


FIG. 5. (Color online) 2D CP spectra in the spectral range of 1.71–2.36 eV. The chirality assignments of RBMs are shown together. In bottom panel, the dotted crisscrossing lines show the relevant vibrational frequencies and resonance energies corresponding to RBMs. The two-way arrows indicate the double-peak structure in the amplitude profile of RBMs. The circles in the top panel show the main features observed in the G mode.
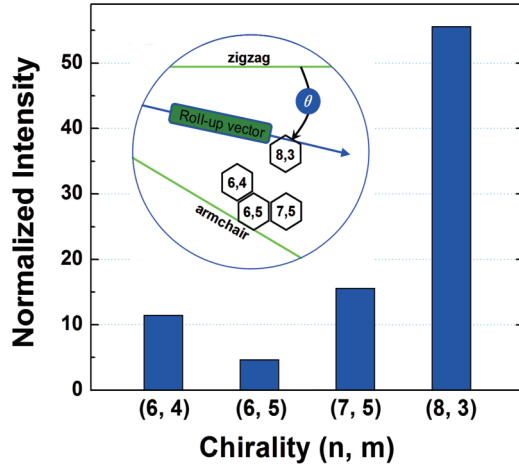
FIG. 6. (Color online) Comparison of the four $E_{22}$ CP intensities between different chiralities $(n, m)$ considering their chirality difference. The inset shows the position of the tubes studied in a chirality map.

Consequently, the vibrational spectra vanish at the center of the "absorbed spectrum," where intense resonant third-order NL interactions are expected to occur. The degree of cancellation depends on the intensity distribution of the probe spectrum, since the modulation varies with the probe spectral intensities at frequencies $\omega_0 - \omega_\nu$ and $\omega_0 + \omega_\nu$. If these two
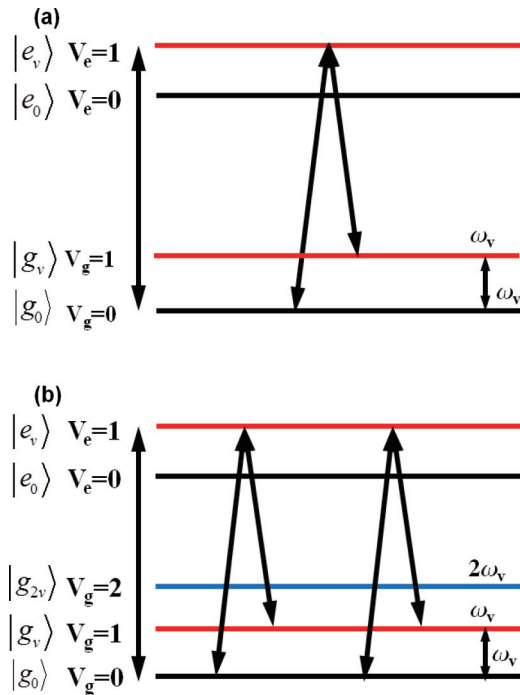


FIG. 7. (Color online) (a) Three-level systems and parameters interacting in the $\Lambda$-type configurations. (b) Five-level systems and parameters interacting in the $\Lambda$-type configuration. $|g_0\rangle$ and $|e_0\rangle$ are the ground electronic state and the lowest electronic excited state with energy $E_0$ and $E_e$, respectively. $|g_\nu\rangle$ and $|g_{2\nu}\rangle$ are the vibrational levels of quantum number $\nu$ and $2\nu$ in the ground electronic states with energy $E_0 + E_\nu$ and $E_0 + 2E_\nu$, respectively. $|e_\nu\rangle$ is the vibrational level of quantum number $\nu$ in the electronic excited state with energy $E_e + E_\nu$.

intensities are the same, they will exactly cancel each other. When the probe spectrum is broad enough, energy will be exchanged. The modulation at the probe frequency $\omega_0 - \omega_\nu$ driven by the resonantly coupled spectral components can trigger oscillations near $\omega_0 - 2\omega_\nu$. Likewise, oscillations can be induced at $\omega_0 + 2\omega_\nu$. Higher order spectral variations can also occur through cascade processes. However, modulations at $\omega_0 \pm n\omega_\nu$ are not due to high-order molecule-field interactions induced by potential anharmonicities such as overtones. (Here we refer to the CNT system as a molecule for simplicity.) On the contrary, the phenomenon arises due to consecutive interactions between the probe and field at different photon energies, even for a harmonic molecular potential. This analysis assumes coherent vibrations in the ground states. Since the interband relaxation occurs with a time constant on the order of 40 fs, the vibrational wave packet contributing to the modulation of the electronic state is attributed to the ground state.[65]

### G. Probe photon energy dependence of the vibrational amplitudes

The probe photon energy dependence of the vibrational amplitude profiles (black lines) of RBMs for the three chiralities (6,4), (6,5), and (8,3) is plotted in Figs. 9(a)–9(c). The amplitude profile for (7,5) is not shown since it is not strong enough for detailed analysis. Several groups have studied RBM amplitude profiles.[28,29,32] In their work, the probe photon energy dependence of the amplitudes was compared with the first derivative of the absorption spectra. It was argued that the resemblance of the amplitude profiles to the first derivative implies wave-packet motion. This type of analysis is hereafter referred to as a DER-type analysis. However, the physical mechanism does not support that conclusion.

Panels (2) in Fig. 9 show a fit of the probe amplitude profiles with the first derivatives of the relevant stationary absorption components (gray lines) for different chiralities. The absorption for each chiral system is obtained from a spectral deconvolution of the stationary absorption spectrum using the Voigt function in Fig. 1(b). The double-peak structure associated with a first-derivative dependence[28,29,32] does not produce a good fit. Even after modifying the absorption components to take into account the errors in fitting the stationary absorption with the analytic function, the disagreement between the calculated derivative function and the probe photon energy dependence remains large. There are substantial deviations in the positions of the valley in the spectra, and even the line shapes of the absolute values of the derivatives and the vibrational amplitudes do not match each other.

It is assumed that no absorption saturation is introduced by the pump laser, as verified by the linear dependence of the signal on the pump intensity. The NL macroscopic polarization $\tilde{P}_{A}^{(3)}(\omega,\tau)$ is induced by three fields, two from the pump pulse $E_{pu}(\omega, \tau)$ and one from probe pulse $E_{pr}(\omega, \tau)$. It can be represented by the following equation as a function of the probe optical frequency $\omega$ and the pump-probe delay time $\tau$,[26,27]

$$\tilde{P}_{A}^{(3)}(\omega,\tau) = \chi_i(\omega)\tilde{E}_{pu}^*\tilde{E}_{pu}\tilde{E}_{pr} \propto I(\omega_0)\tilde{E}_{pr}I_{pu}(\omega). \quad (11)$$
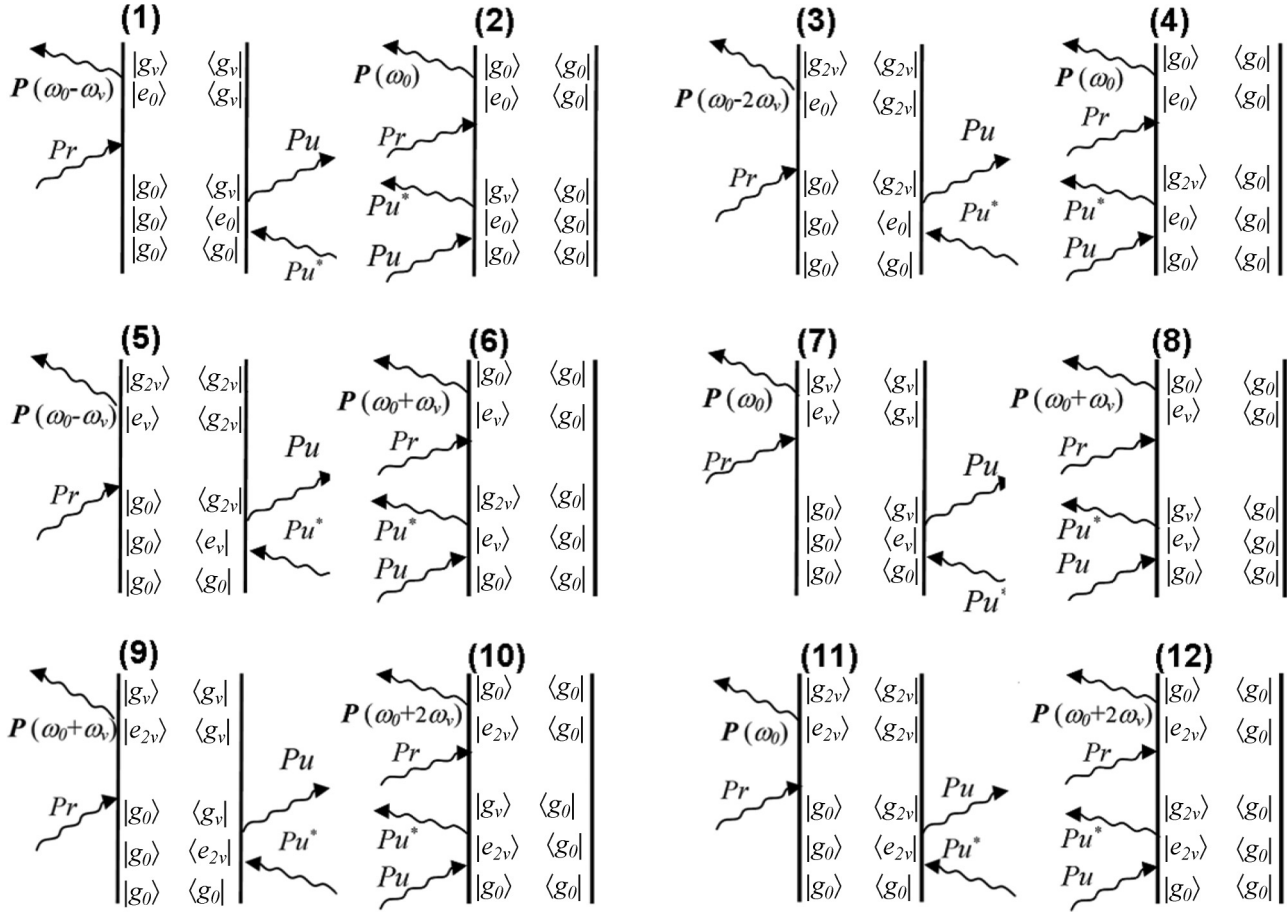
FIG. 8. Double-sided Feynman diagrams of the two nonlinear processes corresponding to ground state bleaching.

The polarization is generated by a Raman gain/loss process associated with energy exchange between the coherent vibrations and the probe optical field, according to the relation $\Delta A(\omega, \tau) \propto -\text{Im}[P^{(3)}(\omega, \tau)/E_{\text{probe}}(\omega, \tau)]$.[26,27] In this process, the probe optical field is alternately deamplified and amplified, depending on the phase change of the vibrations. Thus, the probe photon dependence of the FT power is dependent on the spectral distribution of the laser photons absorbed by the sample. In that case,

$$\Delta A_A(\omega, t) \propto \int d(\omega_0 - \omega_v) \exp(-t/\tau_{2v})$$
$$\times \cos(\omega_v t + \phi_A) I(\omega_0) L_{\text{pu}}(\omega)$$
$$\cong \delta(\omega) \cos(\omega_v t + \phi_A). \quad (12)$$

We next consider a phenomenological analysis. Since the pump laser is resonant with several chiral species, we first separate the spectra associated with each of these species. For quantitative discussion, the phenomenological description of the probe photon energy dependence $\Delta A(\omega_{\text{probe}})$ of the vibrational amplitude can be expressed as[66]

$$\Delta A(\omega_{\text{probe}} = \omega_S) = C_{1S}|a(\omega_{\text{probe}}) - a(\omega_{\text{probe}} - \omega_v)|, \quad (13)$$

$$\Delta A(\omega_{\text{probe}} = \omega_{AS}) = C_{1AS}|a(\omega_{\text{probe}}) - a(\omega_{\text{probe}} + \omega_v)|, \quad (14)$$

$$a(\omega_{\text{probe}}) = L(\omega_{\text{probe}})(1 - 10^{-A\omega_{\text{probe}}}). \quad (15)$$

Here $C_{1S}$ and $C_{1AS}$ are proportionality constants, $\omega_{\text{probe}}$ is the frequency of the probe, $\omega_v$ is the molecular vibration frequency, $L(\omega)$ is the laser spectrum, $a(\omega)$ is the absorbed laser spectrum [which is the frequency distribution of photons being absorbed by the sample, shown by orange lines in panels (1) of Fig. 9], and $A(\omega)$ is the absorbance of the sample at a frequency $\omega$. Equations (14) and (15) correspond to pump/Stokes and pump/anti-Stokes interactions, respectively.

The above calculation is based on the assumption that the imaginary part of the third-order susceptibility $\chi_i^{(3)}$ corresponding to the Raman interaction can be written as

$$\chi_i^{(3)}(-\omega_2 : \omega_1, -\omega_1, \omega_2)$$
$$= C_2(a(\omega_2) - a(\omega_1 = \omega_2 \pm \omega_v)). \quad (16)$$

Here $C_2$ is a proportionality constant, the plus and minus signs correspond to the cases of pump/Stokes and pump/anti-Stokes interactions, respectively, and $\omega_1$ and $\omega_2$ are the components of the probe spectrum. The sideband peaks should occur at frequencies corresponding to the difference between the vibrational frequencies.[25–27]

The energy difference between the sidebands, as numbered in panels (1) of Fig. 9(a), is always found to be close to an integer multiple of the relative RBM frequencies. This observation suggests the presence of overtones in the Raman interactions between the probe pulse and the coherent vibrations. However,
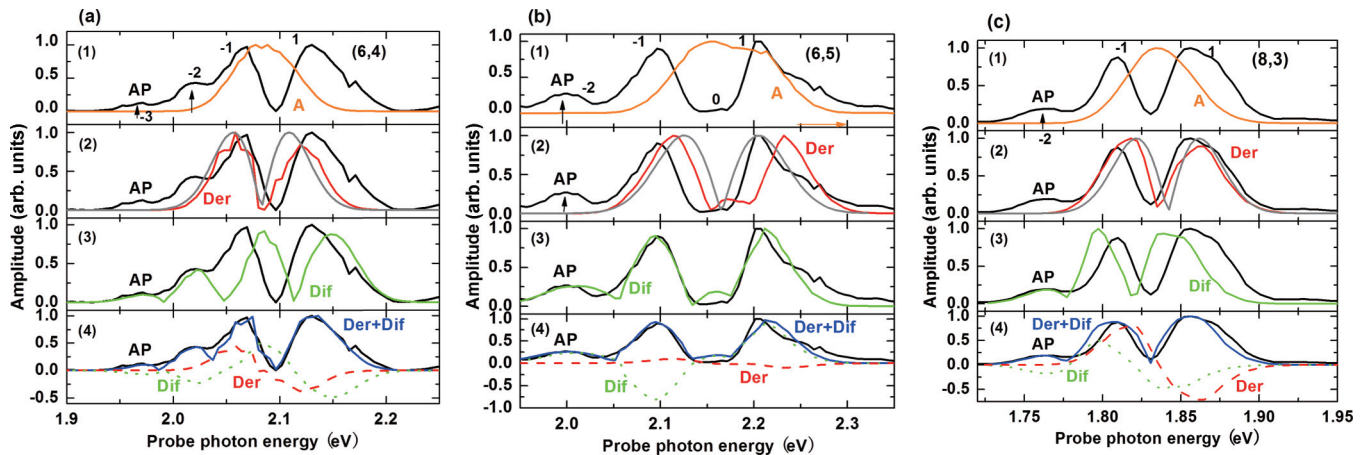
FIG. 9. (Color online) Probe photon energy dependence of normalized RBM amplitude profiles (AP, black lines) for (a) (6,4), (b) (6,5), and (c) (8,3) tubes, fitted with the absorbed laser spectra (A, orange lines), first-derivative of the stationary absorptions (gray lines, panels 2) and absorbed laser spectra (DER, red lines); the absolute difference between the absorbed photon energy distribution by the sample and the distribution shifted by the relevant RBM frequency (DIF, green lines); and the sum of DER and DIF (DER + DIF, blue lines) with relevant contributions, respectively. In the top panels, the arrows indicate the side bands, and the numbers represent the peak number in amplitude profiles. The original DER (dashed red lines) and DIF (dotted green lines) lines in the bottom panels are plotted together before taking absolute value to show their corresponding contributions to the vibrational amplitudes. The amplitude profile of (7,5) is not shown here since it is very weak.

these overtones are not induced by anharmonicity but are instead due to cascaded Raman processes, as discussed below. Because the spectral distribution of the pump and probe lasers is broad, energy exchange can take place between coherent lattice or molecular vibrations and the probe optical field. The interaction can be between the first Stokes beam and the probe beam (the so-called laser used in the discussion of Raman interaction) or between the first Stokes beam and the second (or higher) Stokes beams via the coherent vibrations.

As a result, the probe photon energy dependence can be compared with the absolute value of the difference between the absorbed photon energy spectrum and the distribution shifted by the vibrational frequency, as expressed in Eq. (16). Hereafter, this analysis is referred to as a DIF-type analysis. Fitting of the amplitude profiles with the difference between the shifted and unshifted absorbed probe energy distributions were carried out for Raman ground-state and Raman-like excited-state interactions. They included higher order contributions with adjustable parameters (due, for example, to the phonon amplitudes). The results are plotted in panels (3) of Fig. 9, corresponding to RBMs for (6,4), (6,5), and (8,3) tubes. It can be seen that the fits are still not good.

### H. Fitting the amplitude spectrum with contributions from the real and imaginary parts of the third-order susceptibility

In this section, the fit to the probe photon energy dependence of the vibrational amplitude is improved by combining the contributions from the DIF- and DER-type analyses. In previous papers,[24,28–36] based on the DER analysis, the modulation was explained in terms of a sinusoidal electronic energy modulation due to an RBM-induced change in the diameter of a CNT.[24,28–36] In the following, the mechanism involved in the DER-type contribution is more fully discussed.

A change in the refractive index is induced by the MPM process due to the DER contribution to the modulation.[67] This MPM produces a periodic shift in the probe spectrum. This, in turn, modulates the time-resolved spectrum composed of ground-state absorption bleaching, stimulated emission, and induced absorption. This effect results from the change in refractive index caused by the deformation of the lattice and molecular structure during the coherent vibrations, which the electronic distribution instantaneously follows.[26] The index change introduces a modulation of the probe frequency because of the change in the phase of the probe field, whose time derivative is the optical frequency. Consequently, the signal can be approximated as a spectral shift of the probe pulse induced by a kind of "cross-phase modulation,"[40] and the probe energy dependence of the phonon amplitude follows the first derivative of the electronic resonance.

By adding the contributions from the DIF and DER processes, excellent fits are finally obtained, as shown in panels (4) of Fig. 9. They show the absolute value of the sum (blue lines) of the contributions of the two types of mechanisms for different RBMs with an adjustable relative contribution used as the fitting parameter for DER (dashed lines) and DIF (dotted lines) analyses, before taking absolute values of the sum. We adjusted the relative intensity of different order of phonon peaks taking into accounts of the differences in the signs of amplitudes and add them with the DER profile to make the fitting line shape match the amplitude profile. At first we start with an apparently reasonable ratio to fit with the experimental results of the vibrational amplitude profile. After this we take the sum (over probe photon energy data points) of the squared values of the difference between the fitted and observed values. Then tried to minimize the value by changing the ratios by small amount one after the other to read the minimum deviation. Finally, we take the absolute value. The fitting profiles of DER and DIF types are already

TABLE III. The corresponding parameters used for the fitting of the RBM amplitude profiles, including absorption band center (cm$^{-1}$), shift amounts (cm$^{-1}$) for first-derivative fitting, absorption band width (cm$^{-1}$), FD-type and D-type contributions to the amplitudes (%), and the Stokes ( − ) and anti-Stokes ( + ) order of relevant peaks in amplitude profiles. The zero-order Stokes peaks represent the absorbed laser beam.

| Chirality $(n, m)$ | DER-type Contrib. (%) | Band Center (cm$^{-1}$) | Shift Amount (cm$^{-1}$) | Band Width (cm$^{-1}$) | Shift/ width | DIF-type Contribution (%) | Peak number and its Stokes ( − ) and anti-Stokes ( + ) order | | | |
|---|---|---|---|---|---|---|---|---|---|---|
| (6,4) | ~45% | 16,840 | ~30 | 455.78 | 0.066 | ~55% | +1 | −1 | −2 | −3 |
| (6,5) | ~10% | 17,510 | ~29 | 801.92 | 0.036 | ~90% | 1 | 0 | −1 | −2 |
| (8,3) | ~58% | 14,821 | ~22 | 327.92 | 0.067 | ~42% | 1 | −1 | −2 | / |

shown in panel (4) of Fig. 9 before taking absolute values. For the weight of the DIF and the DER, the fraction (percent) of the contributions from DIF and DER are listed in Table III.

In the cases of the (6,4) and (6,5) tubes, the contributions from the DER analysis are smaller than those from the DIF analysis. In particular, for the (6,5) tubes, the DIF contribution is 90%. The size of the contribution is reversed for the (8,3) tubes, for which more than half is due to the DIF process. The reason for the higher DIF contribution for the (8,3) tubes is the narrower spectral bandwidth of this system compared with the others. The FWHM of the stationary spectra for the (6,4), (6,5), and (8,3) tubes is found from Fig. 1 to be 64.6, 89.9, and 49.2 meV, respectively, as listed in Table I. The order of the widths matches the DIF contributions. It can be concluded that both the DIF and DER analyses make significant contributions to the probe photon energy dependence of the absorbance change, in contrast to previous reports.[28,29,32] The physical mechanisms for the DER and DIF contributions are respectively the real and imaginary parts of the third-order susceptibility. Table III lists the contributing Stokes and anti-Stokes bands for three different chiral systems. Because of the non-uniform probe spectral distribution, the (6,5) and (8,3) tubes show only anti-Stokes sidebands up to second order, while the (6,4) tubes exhibit both Stokes and anti-Stokes bands. The relative sizes of the DER contributions are further discussed below.

From the fitted probe photon energy distributions of the DIF analysis, the Huang-Rhys (HR) factors could be obtained. Since the amplitude of the 0–0 transition energy is reduced by the interference of the Stokes and anti-Stokes interactions, a correct value may not be obtained for the (6,5) case. Instead, the intensity ratios between 0 and 1 and between 1 and 2 were used for the determination of the HR factors for the (6,4) and (6,5) systems, respectively. In the case of the (8,3) tubes, the distributions over 0, 1, and 2 were all used. The HR factors were found to be $0.26 \pm 0.05$, $0.32 \pm 0.05$, and $0.75 \pm 0.04$ for (6,4), (6,5), and (8,3), respectively.

The trends of HR factors can be explained by the stiffness difference of the three SWNT structures. As illustrated in Fig. 10, the expansion in the armchair structure is associated with C–C bond expansion, whereas in the zigzag structure it is associated with C–C–C bending, which is easier than the stretching mode, resulting in a large HR factor. Based on the preceding discussion, the HR factors are predicted to be in the order (6,5) < (6,4) < (8,3) from Fig. 6, since (8,3) is the closest to a zigzag structure among the three, while (6,5) is closest and (6,4) is second closest to an armchair structure. The order of

the (6,4) and (6,5) tubes is reversed in this prediction, but the numerical discrepancy is small.

### I. Size and meaning of the contribution from the real part of the third-order susceptibility

The probe photon energy dependence of the vibrational amplitude exhibits substantial DER contributions. The derivative is the result of a small shift in the spectrum. The size of the shift can be calculated from the derivative with respect to the energy of the original function. However, as shown in Fig. 9 and in the data presented in Refs. 28 and 29, the fits are poor. Therefore, they cannot be reliably used to evaluate the amount
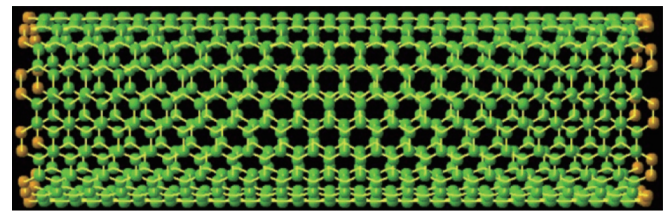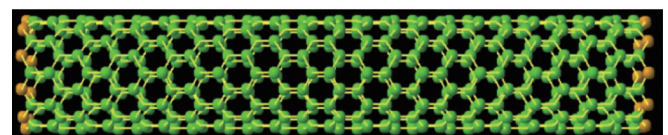


**(10,10) nanotube (armchair)**
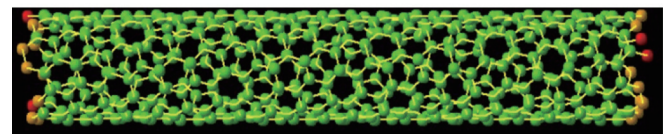


**(8,3) nanotube (chiral)**
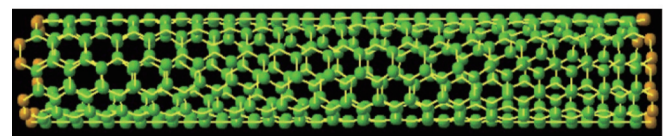


**(6,5) nanotube (chiral)**



**(0,10) nanotube (zig-zag)**

FIG. 10. (Color online) Side views of CNTs with zigzag, chiral, and armchair structures.

of shift. Instead, the shift can be more accurately determined by the moment method. The first moment is defined by

$$M_1(t) = \int_{w1}^{w2} w \Delta A(w) dw \bigg/ \int_{w1}^{w2} \Delta A(w) dw. \quad (18)$$

Here, $w$ is the probe frequency and $\Delta A(w)$ is the difference absorption spectrum due to induced absorption, stimulated emission, and bleaching.

There are three advantages to this moment method compared with the derivative method. The first is that the moment calculation is insensitive to the noise in the signal while the derivative calculation is very sensitive to it. As a result, there is no ambiguity arising from the derivative fitting to the energy dependence of the vibrational amplitude. The second advantage is due to the separation between the apparent transition energy and transition amplitude modulations. The third is the elimination of the contributions of the Raman and Raman-like interactions from wave packets in the ground and excited states. They do not contribute to the first moment if an appropriate integration range is selected, because the Raman contributions are determined by the zeroth moment.[66]

The time-dependent modulation of the difference absorption due to the MPM of each tube can be evaluated by performing a first-moment calculation on the corresponding absorption band in the $\Delta A$ spectrum as a function of sampling time. Figure 11(a) graphs $M_1(t)$ time traces for four spectral components corresponding to the absorption associated with different chiralities. In these time traces, the slow dynamics have been subtracted out to remove the slowly varying contributions from electronic relaxation. After performing a fast FT (FFT), as displayed in Fig. 11(b), two dominant vibrational modes appear in the RBM and G-modes. The vibrational frequencies for the two modes are in good agreement with

those in the 2D display of the CP spectra in Fig. 5; no signal overlap from different chiralities can be observed for RBMs in each time trace. Although there are weak beat patterns in the traces, indicating the presence of a slight superposition of RBM vibrations with different frequencies but similar decay times, tubes of specific chirality dominate the contribution to the first-moment signals.

The results initially appear to indicate that the energy of the $E_{22}$ transition periodically oscillates at the RBM and G-mode frequencies.[28,29] However, this spectral shift, or equivalently the spectral dependence of the DER amplitude, is due to the refractive index modulation by the molecular vibrations. Molecular vibrational modes, such as the RBM, induce changes in the size of the coefficients of the vibrational wave functions with only a few quantum numbers, but represent changes in the vibrational wave function coupled to the electronic wave function, so that the coefficient changes with time. The dynamical process may be stated such that the CNT is a linear combination of several virtual tubes with different diameters proportional to the square root of the vibrational quantum number, $\sqrt{v}$. The vibrational quantum numbers have coefficients determined by the Franck-Condon factors, where the laser spectrum corresponds to the energy $E_{22} + v\hbar\omega_{\mathrm{vib}}$ with electronic energy $E_{22}$ and vibrational energy $v\hbar\omega_{\mathrm{vib}}$, where $v = 0, 1$, and 2. Thus, the diameter does not change continuously as proposed in previous papers[28,29] but instead varies discretely as a linear combination of several different diameters.

### J. RBMs studied by the moment calculation

The method by which the CPs modulate the time-resolved spectrum is next discussed, after clarifying that the CP packet wave function is given by a linear combination of eigenmodes.
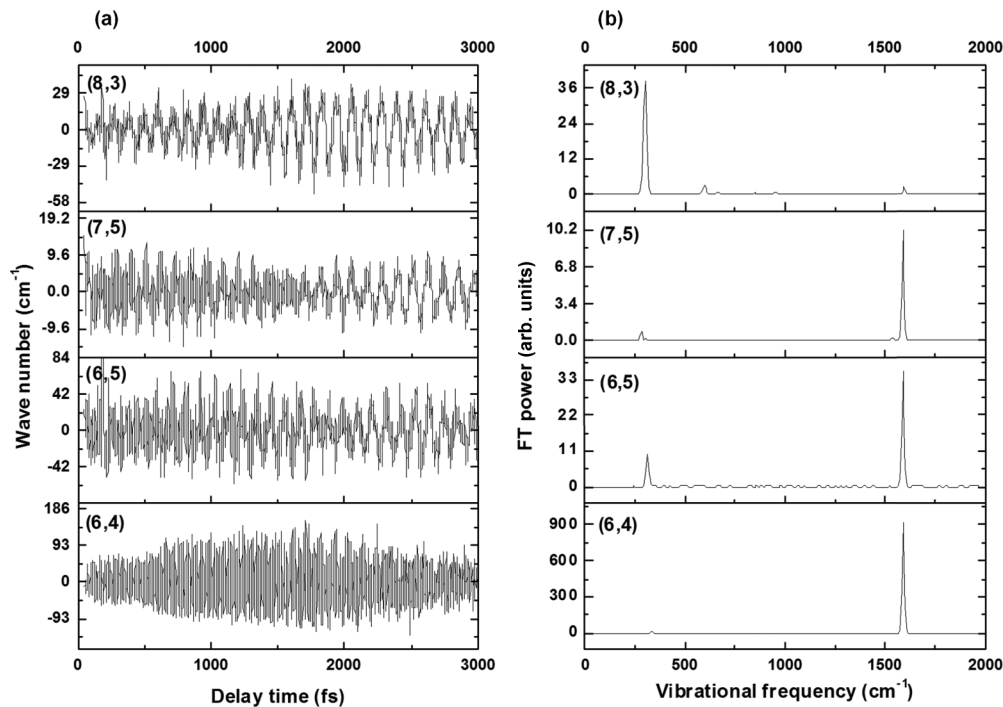


FIG. 11. (a) The dynamics of the first moment, $M_1(t)$, of (8,3), (7,5), (6,5), and (6,4) chiral systems tracked as a function of the pump-probe delay time. (b) The FFT power spectra of the first moment $M_1(t)$.
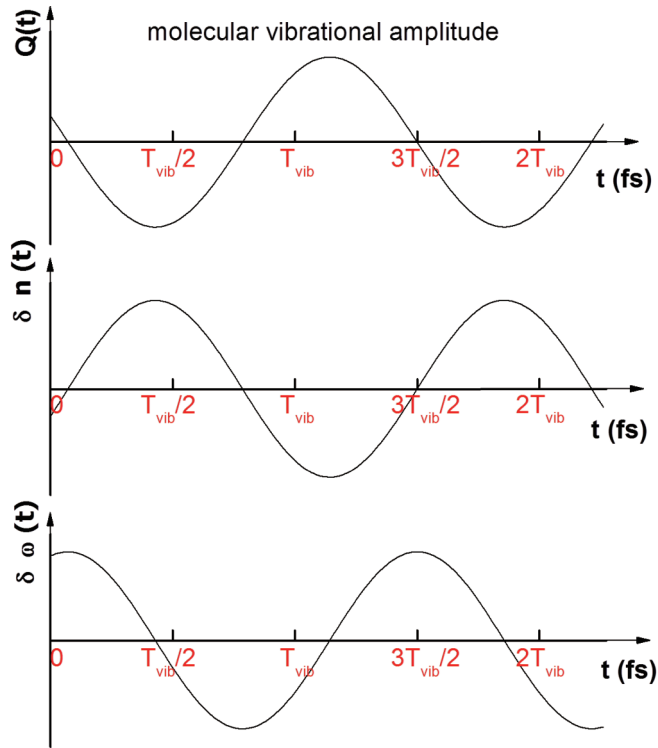
FIG. 12. (Color online) Classical views of displacement coordinate $Q(t)$ of a CNT tube from the equilibrium state as a function of time in the ground state, and corresponding time evolution in the refractive index, $\Delta n(t)$ and resulting probe frequency shift $\Delta\omega(t)$ as a function of time. $T_{\text{vib}}$ is vibrational period of CP.
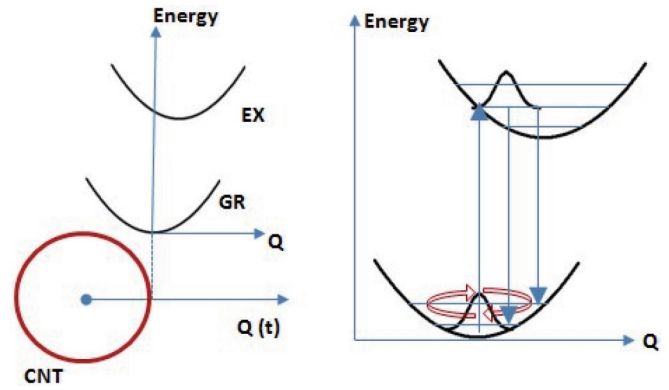


FIG. 13. (Color online) Schematics of the potential curve along the displacement with the origin of equilibrium position of the radial coordinate starting from the symmetric center (not the origin) of the CNT. The arrows schematically show the motion of the wave packet along the potential curve with schematic vibrational levels.

One might wonder whether the refractive index change can be expressed as a linear combination of the vibronic wave function, such that the refractive index would have a steplike structure. In fact, even though the change in the spectral shape of the probe field induced by CPs is separated by the vibrational frequency, the phase modulation spectrum is smooth and continuous because of the characteristics of the Kramers-Kronig relations. The nonresonant contribution can dominate the refractive index spectrum of the relevant chiral system in the resonant region, together with a significant contribution from other chiral species having nearby resonant peaks. This behavior was already observed in a one-dimensional system of J-aggregated molecules.[66] Accordingly, the spectral shift due to the refractive index modulation is so small that the index changes can be considered to be linear with respect to the probe spectral changes. Therefore, the MPM mechanism can be depicted in the classical way using $Q(t)$, as shown in Fig. 12. The displacement $Q(t)$ of the radial axis of a CNT from its equilibrium position is not described by a single sharp line but instead by several (two or three) lines with some probability distribution. This is because of the wave function of the CP is expressed by the linear combination of wave functions of several vibrational quantum number. The potential curves in the ground and excited states along the CNT diameter have minima at the equilibrium positions in the ground state, as illustrated in Fig. 13. It shows schematically the generation of wave-packet motion in the ground state. In the excited state the lifetime (50–90 fs) is not long enough to establish a well-defined frequency of the breathing mode (~100 fs),

along which coordinate the wave packet moves for long time enough.

The corresponding time evolution of the refractive index and resulting probe frequency shift are also shown in Fig. 12. The lines, as mentioned above, may have some distribution along the ordinate $\Delta n(t)$ and $\Delta\omega(t)$ axes with single peaks, but they are not separated as in the DIF case. Because of the Kramers-Kronig relations, if an energy shift takes place, the spectra of both the absorption and refractive index move in the same direction. The electronic distribution follows the nuclear motion and hence the instance of the maximum diameter the electronic density is lowest along the periphery of the tube. This corresponds to the turning point of the nuclear wave packet on the ground-state potential curve. Then the refractive index becomes smallest because of minimum polarizability at the optical frequency. Hence $\delta n(t)$ shows $\pi$ out of phase shift from that of $Q(t)$, as shown in Fig. 12. Since the instantaneous frequency ($\omega + \delta\omega$) of optical field is given by the time derivative of electric field, $\delta\omega$ has $\pi/2$ shift from $\delta n(t)$, as depicted in the figure.

The NL refractive index due to the molecular vibration is determined by $\delta n = n_2 I$, where $I$ is the peak intensity of the focused pump laser on the sample surface at the relevant transition energy of the corresponding chiral system. The values of $\delta n$ for the four chiral systems were calculated using the relation $\delta\omega/\omega_E \approx \delta n/n$ in terms of the standard deviation of the probe frequency modulation ($\delta\omega$) and of the electronic transition frequency ($\omega_E$). The resulting values for the effective NL refractive index of the four modes due to MPM are listed in Table IV, together with the pump intensity $I$ at the relevant transition energy. Here again, the value for (8,3) tubes is much larger than that for (6,5) tubes, because the former have a much larger DER contribution (58%) than the latter (10%), according to Table III. The effective NL refractive index due to the RBM was determined to be in the range 0.2 to 3.1 $\times$ $10^{-17}$ cm$^2$/W for each system.

Finally, consider the three differences between the present discussion and the theory by Sanders *et al.*[30] The first is that Sanders treated the system in terms of a displacement potential upon excitation and thus it does not include Raman processes.

TABLE IV. Vibration-induced nonlinear refractive index change estimated by analyzing the first-moment dynamics. $\omega_E$: transition energy; $\omega_R$: RBM frequency; $\omega_G$: G mode frequency; $\Delta\omega_R$: the root mean square magnitude of the frequency modulation of RBM; $\Delta\omega_G$: the root mean square of the frequency modulation of G-mode; $n_2$: nonlinear refractive index determined by the equations of refractive index change due to molecular vibration, $\delta n = n_2 I$ and $\delta\omega/\omega_{R(G)} \sim \delta n/n$, and $I$ is the peak intensity of focused pump laser on the sample surface at the relevant transition energy of the corresponding chiral system.

| Chirality $(n, m)$ | $\omega_E$ (cm$^{-1}$) | $\omega_{RBM}$ [$\phi$(phase($\pi$)] (cm$^{-1}$) | $\Delta\omega_R$ (RBM) (cm$^{-1}$) | $\Delta\omega_R/\omega_E$ (RBM) (10$^{-4}$) | $I$ (10$^{10}$W/cm$^2$) | $n_2$ (RBM) (10$^{-17}$cm$^2$/w) |
|---|---|---|---|---|---|---|
| (6,4) | 16,855 | 337 (0.48) | 10.93 | 6.48 | 0.99 | 0.66 |
| (6,5) | 17,462 | 310 (0.07) | 17.22 | 9.86 | 4.71 | 0.21 |
| (7,5) | 15,349 | 282 | 12.14 | 7.91 | 0.71 | 1.11 |
| (8,3) | 14,892 | 301(0.05) | 30.60 | 20.5 | 0.66 | 3.09 |

This fact is evident in Figs. 14 and 19 of their paper, in which the CP vibration appears in the form of a cosine function with a delay due to the finite pulse duration. Accordingly, their assignment of the signal is in terms of Raman generation of a wave packet in the excited state, but it excludes Raman generation in the ground state. The second difference is that they described the CP dynamics semiclassically as seen in the same figures with a continuous displacement associated with the CP motion. Third, the real part of the nonlinearity is not included in their analysis. In addition, the effect of signal modulation due to MPM, which typically appears in impulsive excitations, is not included.

## IV. CONCLUSIONS

CP and electronic relaxation dynamics of SWNTs were investigated for the four chiral systems (6,4), (6,5), (7,5), and (8,3) in CoMoCat-grown ensembles, using a sub-10-fs broadband visible pulse and a high-sensitivity detection system based on a 128-channel lock-in amplifier. From the measured data on the probe energy-dependent amplitudes of the RBMs, it was found that the imaginary and real parts of the third-order susceptibility both play important roles in the modulation of the difference absorbance. The amplitude profiles of RBMs can be accurately fit by the sum of the first derivative of the absorption due to the real part of the third-order susceptibility and the difference absorption due to the imaginary part of the susceptibility induced by a Raman process, with the relative contributions being adjustable. The imaginary part, given by a DIF contribution in the fit, arises from energy exchange between CPs and the probe optical field. The size of the HR factors obtained from DIF fits to the (6,4), (6,5), and (8,3) systems are estimated to be 0.26, 0.32, and 0.75, respectively; they depend on the stiffness of the CNT structure. The real part, resulting from a refractive index change due to molecular vibrations, manifests itself as DER dependence due to the MPM process. The NL refractive index for each chiral system is determined to be in the range of 0.2 to 3.1 $\times$ 10$^{-17}$ cm$^2$/W.

*Corresponding author: kobayashi@ils.uec.ac.jp

†Corresponding author: niezg@ils.uec.ac.jp

[1] S. Iijima, Nature (London) **354**, 56 (1991).

[2] M. S. Dresselhaus, G. Dresselhaus, and P. Avouris, (eds.), *Carbon Nanotubes: Synthesis, Structure, Properties and Applications* (Springer, Berlin, 2001).

[3] M. Dresselhaus, *Carbon Nanotubes: Synthesis, Structure, Properties, and Applications* (Springer, New York, 2001).

[4] R. Saito, G. Dresselhaus, and M. Dresselhaus, *Physical Properties of Carbon Nanotubes* (World Scientific, Singapore, 2003).

[5] P. Harris, *Carbon Nanotubes and Related Structures: New Materials for the Twenty-First Century* (Cambridge University Press, Cambridge, England, 1999).

[6] T. Kobayashi, M. Yoshizawa, U. Stamm, M. Taiji, and M. Hasegawa, J. Opt. Soc. Am. B **7**, 1558 (1990).

[7] T. Kobayashi, *J-aggregates* (World Scientific, Singapore, 1996).

[8] B. J. LeRoy, S. G. Lemay, J. Kong, and C. Dekker Nature **432**, 371 (2004).

[9] H. Htoon, M. J. O'Connell, S. K. Doorn, and V. I. Klimov, Phys. Rev. Lett. **94**, 127403 (2005).

[10] V. Perebeinos, J. Tersoff, and P. Avouris, Phys. Rev. Lett. **94**, 027402 (2005).

[11] A. Dyatlova, C. Köhler, E. Malic, J. Gomis-Bresco, J. Maultzsch, A. Tsagan-Mandzhiev, T. Watermann, A. Knorr, and U. Woggon, Nano Lett. **12**, 2249 (2012).

[12] C. V. Shank, R. Yen, R. L. Fork, J. Orenstein, and G. L. Baker, Phys. Rev. Lett. **49**, 1660 (1982).

[13] S. Adachi, V. M. Kobryanskii, and T. Kobayashi, Phys. Rev. Lett. **89**, 027401 (2002).

[14] Y. Yin, A. G. Walsh, A. N. Vamivakas, S. B. Cronin, D. E. Prober, and B. B. Goldberg, Phys. Rev. B **84**, 075428 (2011).

[15] S. Reich, C. Thomsen, and J. Robertson, Phys. Rev. Lett. **95**, 077402 (2005).

[16] C. D. Spataru, S. Ismail-Beigi, L. X. Benedict, and S. G. Louie, Phys. Rev. Lett. **92**, 077402 (2004).

[17]F. Wang, G. Dukovic, L. E. Brus, and T. F. Heinz, Science **308**, 838 (2005).

[18]A. Srivastava, H. Htoon, V. I. Klimov, and J. Kono, Phys. Rev. Lett. **101**, 087402 (2008).

[19]A. Jorio, R. Saito, J. H. Hafner, C. M. Lieber, M. Hunter, T. McClure, G. Dresselhaus, and M. S. Dresselhaus, Phys. Rev. Lett. **86**, 1118 (2001).

[20]A. Jorio, M. A. Pimenta, A. G. S. Filho, R. Saito, G. Dresselhaus, and M. S. Dresselhaus, New J. Phys. **5**, 139 (2003).

[21]S. K. Doorn, D. A. Heller, P. W. Barone, M. L. Usrey, and M. S. Strano, Appl. Phys. A: Mater. Sci. Process. **78**, 1147 (2004).

[22]J. Jiang, R. Saito, G. G. Samsonidze, A. Jorio, S. G. Chou, G. Dresselhaus, and M. S. Dresselhaus, Phys. Rev. B **75**, 035407 (2007).

[23]J. Jiang, R. Saito, K. Sato, J. S. Park, G. G. Samsonidze, A. Jorio, G. Dresselhaus, and M. S. Dresselhaus, Phys. Rev. B **75**, 035405 (2007).

[24]A. Gambetta, C. Manzoni, E. Menna, M. Meneghetti, G. Cerullo, G. Lanzani, S. Tretiak, A. Piryatinski, A. Saxena, R. L. Martin, and A. R. Bishop, Nat. Phys. **2**, 515 (2006).

[25]T. Kobayashi, J. Zhang, and Z. Wang, New J. Phys. **11**, 013048 (2009).

[26]T. Kobayashi and Z. Wang, IEEE J. Quantum Electron. **44**, 1232 (2008).

[27]N. Ishii, E. Tokunaga, S. Adachi, T. Kimura, H. Matsuda, and T. Kobayashi, Phys. Rev. A **70**, 023811 (2004).

[28]Y. S. Lim, K.-J. Yee, J. H. Kim, E. H. Hároz, J. Shaver, J. Kono, S. K. Doorn, R. H. Hauge, and R. E. Smalley, Nano Lett. **6**, 2696 (2006).

[29]J. H. Kim, K.-J. Han, N. J. Kim, K. J. Yee, Y. S. Lim, G. D. Sanders, C. J. Stanton, L. G. Booshehri, E. H. Hároz, and J. Kono, Phys. Rev. Lett. **102**, 037402 (2009).

[30]G. D. Sanders, C. J. Stanton, J. H. Kim, K. J. Yee, Y. S. Lim, E. H. Hároz, L. G. Booshehri, J. Kono, and R. Saito, Phys. Rev. B **79**, 205434 (2009).

[31]K. Kato, K. Ishioka, M. Kitajima, J. Tang, R. Saito, and H. Petek, Nano Lett. **8**, 3102 (2008).

[32]L. Lüer, C. Gadermaier, J. Crochet, T. Hertel, D. Brida, and G. Lanzani, Phys. Rev. Lett. **102**, 127401 (2009).

[33]K. Makino, A. Hirano, K. Shiraki, Y. Maeda, and M. Hase, Phys. Rev. B. **80**, 245428 (2009).

[34]Y. S. Lim, J. G. Ahn, J. H. Kim, K. J. Yee, T. Joo, S. H. Baik, E. H. Hàroz, L. G. Booshehri, and J. Kono, ACS Nano **4**, 3222 (2010).

[35]J. Wang, M. W. Graham, Y. Z. Ma, G. R. Fleming, and R. A. Kaindl, Phys. Rev. Lett. **104**, 177401 (2010).

[36]Z. Zhu, J. Crochet, M. S. Arnold, M. C. Hersam, H. Ulbricht, D. Resasco, and T. Hertel, J. Phys. Chem. C **111**, 3831 (2007).

[37]W. T. Pollard, S.-Y. Lee, and R. A. Mathies, J. Chem. Phys. **92**, 4012 (1990).

[38]W. T. Pollard, H. L. Fragnito, J.-Y. Bigot, C. V. Shank, and R. A. Mathies, Chem. Phys. Lett. **168**, 239 (1990).

[39]R. R. Alfano and S. L. Shapiro, Phys. Rev. Lett. **24**, 592 (1970).

[40]M. N. Islam, L. F. Mollenauer, R. H. Stolen, J. R. Simpson, and H. T. Shang, Opt. Lett. **12**, 625 (1987).

[41]T. N. Kumar, F. Rosca, A. Widom, and P. M. Champion, J. Chem. Phys. **114**, 701 (2001).

[42]T. N. Kumar, F. Rosca, A. Widom, and P. M. Champion, J. Chem. Phys. **114**, 6795 (2001).

[43]T. Dumitrică, M. E. Garcia, H. O. Jeschke, and B. I. Yakobson, Phys. Rev. Lett. **92**, 117401 (2004).

[44]T. Dumitrică, M. E. Garcia, H. O. Jeschke, and B. I. Yakobson, Phys. Rev. B, **74**, 193406 (2006).

[45]H. O. Jeschke, A. H. Romero, M. E. Garcia, and A. Rubio, Phys. Rev. B, **75**, 125412 (2007).

[46]I. Iwakura, A. Yabushita, and T. Kobayashi, J. Am. Chem. Soc. **131**, 688 (2009).

[47]I. Iwakura, A. Yabushita, and T. Kobayashi, Chem. Phys. Lett. **501**, 567 (2010).

[48]A. Shirakawa, I. Sakane, M. Takasaka, and T. Kobayashi, Appl. Phys. Lett. **74**, 2268 (1999).

[49]A. Baltuška, T. Fuji, and T. Kobayashi, Opt. Lett. **27**, 306 (2002).

[50]M. S. Arnold, S. I. Stupp, and M. C. Hersam, Nano Lett. **5**, 713 (2005).

[51]S. M. Bachilo, L. Balzano, J. E. Herrera, F. Pompeo, D. E. Resasco, and R. B. Weisman, J. Am. Chem. Soc. **125**, 11186 (2003).

[52]Y. Miyata, K. Yanagi, Y. Maniwa, T. Tanaka, and H. Kataura, J. Phys. Chem. C **112**, 15997 (2008).

[53]See Supplemental Material at http://link.aps.org/supplemental/10.1103/PhysRevB.88.035424 for sample morphology.

[54]S. M. Bachilo, M. S. Strano, C. Kittrell, R. H. Hauge, R. E. Smalley, and R. B. Weisman, Science **298**, 2361 (2002).

[55]R. Bruce Weisman and Sergei M. Bachilo, Nano Lett. **3**, 1235 (2003).

[56]C. Fantini, A. Jorio, M. Souza, M. S. Strano, M. S. Dresselhaus, and M. A. Pimenta, Phys. Rev. Lett. **93**, 147406 (2004).

[57]H. Telg, J. Maultzsch, S. Reich, F. Hennrich, and C. Thomsen, Phys. Rev. Lett. **93**, 177401 (2004).

[58]J. Maultzsch, H. Telg, S. Reich, and C. Thomsen, Phys. Rev. B **72**, 205438 (2005).

[59]Y. Kim, N. Minami, and S. Kazaoui, Appl. Phys. Lett. **86**, 073103 (2005).

[60]W. G. Wildöer, L. C. Venema, A. G. Rinzler, R. E. Smalley, and C. Dekker, Nature (London) **391**, 59 (1998).

[61]T. W. Odom, J. L. Huang, P. Kim, and C. M. Lieber, Nature (London) **391**, 62 (1998).

[62]J. S. Lauret, C. Voisin, G. Cassabois, C. Delalande, Ph. Roussignol, O. Jost, and L. Capes, Phys. Rev. Lett. **90**, 057404 (2003).

[63]G. W. Chantry, in *The Raman Effect: Principles*, edited by A. Anderson, Vol. 1 (Marcel Dekker, New York, 1971), pp. 287–342.

[64]J. Du, K. Nakata, Y. Jiang, E. Tokunaga, and T. Kobayashi, Biophys. J. **101**, 995 (2011).

[65]C. Manzoni, A. Gambetta, E. Menna, M. Meneghetti, G. Lanzani, and G. Cerullo, Phys. Rev. Lett. **94**, 207401 (2005).

[66]Y. Wang and T. Kobayashi, Chem. Phys. Chem. **11**, 889 (2010).

[67]N. Zhavoronkov and G. Korn, Phys. Rev. Lett. **88**, 203901 (2002).